P2.67

Modelling the Transient Response of the Dines Anemometer in Tropical Cyclone Winds

Jeffrey D. Kepert
Centre for Australian Weather and Climate Research,
Bureau of Meteorology, 700 Collins St, Melbourne Vic 3000.
Email: J.Kepert@bom.gov.au

29th AMS Conference on Hurricanes and Tropical Meteorology, Tucson, Arizona, May 10 – 14, 2010.

1. Introduction

The Dines, or pressure-tube, anemometer, consists of a large-diameter pitot tube mounted on a vane, connected to a unique manometer. This manometer consists of an open-bottomed tapered float in a water tank, with the pressure tube from the pitot head feeding into the air space in the float. As the wind speed rises, the pressure inside the float increases and the float rises, moving the recording pen. Further information on the instrument may be found in Dines (1892) and Gold (1936). The Dines anemometer is now obsolete in Australia, having been largely replaced by cup anemometers. Nevertheless, historical records from the instrument are important to understanding the wind risk climate, not least since the two strongest gusts ever recorded on the Australian mainland, in Tropical Cyclones Tracy of 1974 and Vance of 1999, were on Dines instruments.

The behaviour of cup anemometers in turbulence has been extensively studied, but comparatively little similar work has been done on the Dines, and none recently. Some studies have compared cup to Dines anemometers (e.g. Mattice 1938; Dyck 1941; Handcock 1963; Logue 1986; Smith 1981) or looked at the Dines anemometer in isolation (e.g. Wieringa 1980; Bureau of Meteorology 1987) but these have mostly focussed on the mean, rather than the transient, response. Here, we present and analyse a newly developed physical model of the transient response of the Dines anemometer. Two previously observed resonances are confirmed, and their physical mechanism described. A third low-frequency oscillation, not previously known, is found in the model. Observations that may indicate this oscillation are briefly discussed. In addition, it is shown that the instrument may overspeed, albeit for different reasons to cup anemometers.

Further work, in collaboration with the Cyclone Testing Stations at James Cook University and Geosciences Australia, will involve verification and calibration of the physical model by experiments on a remnant functioning Dines instrument, and reinterpretation of the historic gust record.

2. Modelling the Float Chamber

The manometer of the Dines anemometer is illustrated in Fig. 1 has a complicated geometry, designed to produce a steady-state float displacement that is linear in the applied wind speed. This geometry complicates the analysis, so for convenience a simpler geometry will be temporarily assumed. In particular, the following simplifying assumptions are made:

1. The cross-sectional areas of the water inside and outside of the float are equal.

2. The float and containing vessel have parallel sides.

3. The pressure in the suction chamber is constant, or equivalently, the suction chamber is open to the atmosphere.

4. The movement of the float and liquid experience Newtonian damping with time-scales τ_1 and τ_2 respectively.

5. The relative motion of the float and liquid is Newtonian damped with time-scale τ_3, to represent the choke at the bottom of the float (see section 2.4.

With these assumptions, the float chamber is *nearly* equivalent to a U-tube manometer with a frictionless piston supported by some trapped air in one arm, and forced by varying the amount of trapped air. Figure 1 sketches the successive approximations, from tapered float, to parallel-sided float, to U-tube. In the U-tube, the piston represents the Dines float and the manometer liquid the water in the Dines float chamber. The trapped air between the piston and the manometer liquid corresponds to that inside the Dines float. It is assumed to compress isothermally, and acts as a spring between the two masses.

An important difference with the Dines manometer is that the simplified system does not measure pressure. In a Dines manometer, the net upwards force on the float decreases as the float rises, because the area of the water surface in the bottom of the tapered float diminishes. In contrast, a parallel-sided float will rise indefinitely given an infinite supply of internal air at a fixed pressure, provided that the pressure is sufficient to lift the float. Hence the forcing in this system is better regarded as being the mass of trapped air, rather than its pressure. This simplification is helpful for understanding the transient response, but will later be removed. The mass of air in the chamber will continue to be a key variable in the system, but this mass will be eventually governed by equations which describe the flow of air between the anemometer head and the chamber via the tubing.

A second difference is that the flow of the liquid around the bottom of the Dines float is probably rather complex, while the analogous flow around the bend in the U-tube is much more simply modelled. In particular, the liquid will be assumed to move as a single mass.

The variables in the system are the positions and velocities of the piston and manometer liquid, (x_1, v_1) and (x_2, v_2) respectively, and the pressure p of the trapped air. The independent variables are the piston mass m_1, the tube area A, the amount of trapped air $c(t)$, the pressure of air in the suction chamber p_{env}, and the mass of the liquid $m_2 = 2x_eA\rho$ where x_e is the resting position of the liquid if the piston was removed and ρ is its density. All distances are measured along the tube from the bottom of the U; distances towards the piston side are positive.

The trapped air has mass m_a, pressure $p_{env} + p$ and density ρ_a. Combining the definition of density $m_a = (x_1 - x_2)A\rho_a$ with the gas law $p_{env} + p = \rho_a R_d T$ yields

$$c(t) \equiv R_d T m_a(t) = (p_{env} + p)A(x_1 - x_2)$$

where R_d is the gas constant for dry air and T is the air temperature. We will use $c(t)$ as the principal forcing of the system.

The forces on the float are its weight gm_1, the net upwards pressure due to the trapped air pA, and friction which we model as a linear damping to zero with time scale τ_1, and a linear damping to the liquid motion with time scale τ_3. Newton's second law gives

$$m_1\dot{v}_1 = pA - gm_1 - m_1\tau_1 v_1 - m_1\frac{\tau_3}{2}(v_1 - v_2)\,.$$

The liquid motion is forced by the air pressure difference p between the chamber and outside, and by the hydrostatic pressure difference $2(x_e - x_2)\rho g$ due to the different liquid levels inside and outside of the float. A linear damping is again included. It is assumed that the water moves essentially as a solid mass, hence

$$2x_eA\rho\dot{v}_2 = -pA + 2(x_e - x_2)A\rho g - 2x_eA\rho\tau_2 v_2 - 2x_eA\rho\frac{\tau_3}{2}(v_2 - v_1)\,.$$

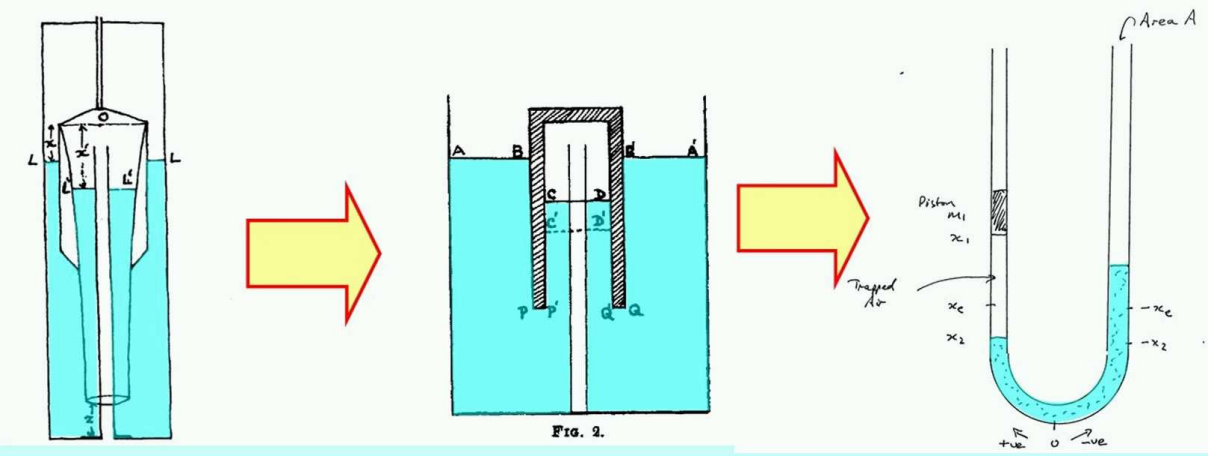

Figure 1: The Dines anemometer float chamber and successive approximations. The left panel shows the classic Dines manometer, with the float of tapered cross-section designed to produce a displacement that is linear in wind speed. The central tube feeds the pressure at the pitot tube entry into the interior of the float. Blue shading represents water. The middle panel approximates the float as having parallel sides. The right panel has similar topology to the other panels, but approximates the liquid as moving as a single mass in a U-tube. The float is represented as a piston in one arm of the tube, supported above the liquid by the trapped air. The notation is that x_1 represents the position of the piston, x_2 the position of the liquid top in the piston arm, and x_e the equilibrium position that the liquid would take if the piston was removed. Distances are measured from the bottom of the U-tube, with the piston arm being positive. The left and centre drawings are from Gold (1936).

where $2x_eA\rho$ is the mass of the liquid. This last assumption is not unduly restrictive – if the channel through which the water moves is not of constant cross-section, then the greater mass per unit length in the wider sections will be exactly compensated by the lower acceleration experienced by water therein – it is the inertia that matters.

In summary, the equations governing the system are

$$x_1 - x_2 = \frac{c(t)}{A(p + p_{env})} \tag{1}$$

$$\dot{x}_1 = v_1 \tag{2}$$

$$\dot{v}_1 = \frac{pA}{m_1} - g - \tau_1 v_1 - \frac{\tau_3}{2}(v_1 - v_2) \tag{3}$$

$$\dot{x}_2 = v_2 \tag{4}$$

$$\dot{v}_2 = \frac{-pA + 2(x_e - x_2)A\rho g}{2x_eA\rho} - \tau_2 v_2 - \frac{\tau_3}{2}(v_2 - v_1) \tag{5}$$

Equation (1) is Boyle's law and (3) and (5) are Newton's second law. Equation (1) is used to eliminate pA from the remaining equations, leaving a set of four nonlinear coupled differential equations. Linear analytic solutions and numerical solutions (by fourth-order Runge-Kutta integration) will be obtained.

The equilibrium state of the system is found by solving $\dot{v}_1 = \dot{v}_2 = 0$ with $c = c_0$ constant, giving

$$x_{2e} = x_e - \frac{m_1}{2A\rho} \tag{6}$$

$$x_{1e} = x_{2e} + \frac{c_0}{gm_1} \tag{7}$$

Note that the equilibrium water level (6) is independent of c_0, as in a real Dines anemometer (Gold 1936).

The *calibration* of the system, practically speaking, is the readings x_1 and x_2 that it would produce in response to steady forcing c_0, provided that sufficient time had elapsed for it to reach equilibrium $v_1 = v_2 = 0$. In the absence of damping, total energy is conserved and so this state will never be met, but in reality, the anemometer will tend to this state. It is convenient to be able to discuss the calibration with respect to nonsteady forcing. Hence (6) and (7), the calibration equations of the system, will also be applied to nonsteady forcing $c(t)$, so as to compare the instantaneous readings of the instrument to that it would give in a steady state with that instantaneous forcing held constant. In particular, this interpretation is necessary for the analysis of "overshooting" and "undershooting" of gust measurements in unsteady flow.

The energy within the system for steady $c = c_0$ is given by

$$E_K = \frac{1}{2} m_1 v_1^2 + x_e A \rho v_2^2 \tag{8}$$

$$E_{P,1} = m_1 (x_1 - x_{1e}) g \tag{9}$$

$$E_{P,2} = A\rho g \left[(x_2 - x_e)^2 - (x_{2e} - x_e)^2 \right] \tag{10}$$

$$E_{P,p} = c_0 \log \left(\frac{x_1 - x_2}{x_{1e} - x_{2e}} \right) + p_{env} A [(x_1 - x_2) - (x_{1e} - x_{2e})] \tag{11}$$

representing respectively the kinetic energy E_K, the potential energies due to the positions of the piston $E_{P,1}$ and liquid $E_{P,2}$, and the potential energy due to the pressure of the trapped air $E_{P,p}$. These potential energies are relative to the equilibrium states. The accuracy of the numerical solutions was checked by requiring them to conserve total energy to high accuracy in simulations with damping $\tau_1 = \tau_2 = \tau_3 = 0$.

2.1 *Undamped behaviour*

Some limiting, small-amplitude undamped cases for steady forcing, $c = c_0$, are of interest. The first three are not very useful in understanding the numerical solutions, but the fourth will be seen to be of significant importance. For simplicity we take $p_{env} = 0$ here; this simplification is relaxed in section 2.3.

1. *Liquid stationary.* Then write $x_1 = x_2 + c_0/(gm_1) + \epsilon$, where the constant $c_0/(gm_1)$ is motivated by (7). Equations (2) and (3) with $\tau_1 = \tau_2 = \tau_3 = 0$ give

$$\ddot{\epsilon} = g \left(1 + \frac{g m_1}{c_0} \epsilon \right)^{-1} - g \tag{12}$$

$$\approx -\frac{g^2 m_1}{c_0} \epsilon \tag{13}$$

   which describes a simple harmonic oscillator with frequency

$$f_1 = g \sqrt{\frac{m_1}{c_0}}. \tag{14}$$

   This limit will also describe the motion of the piston relative to the liquid when the liquid is moving relatively slowly, or when the liquid is much more massive than the float. Physically, it is a mode in which the piston "bounces" on the trapped air.

2. *Piston mass negligible.* Equations (4) and (5) become

$$\ddot{x}_2 = -\frac{g}{x_e} x_2 + g \tag{15}$$

   which in which the liquid oscillates with frequency

$$f_2 = \sqrt{\frac{g}{x_e}} \tag{16}$$

about mean position x_e. This is a gravitational mode.

3. *Piston and liquid move together* That is, $v_1 = v_2$, which is the same as the previous case, except that the oscillating mass has increased by m_1. The frequency is

$$f_3 = \left(\frac{2A\rho g}{2x_e A\rho + m_1} \right)^{1/2}. \tag{17}$$

This is also a gravitational mode.

4. *Coupled oscillations.* Consider oscillations of the form

$$x_1(t) = x_{1e} + \delta b e^{i\omega t} \tag{18}$$
$$x_2(t) = x_{2e} + \delta e^{i\omega t} \tag{19}$$

where $i^2 = -1$. That is, the piston and liquid are oscillating with the same frequency ω, and b describes the relative amplitude and phase of the oscillations. Substituting these equations into the governing equations (1) to (5), expanding as a Taylor series in δ and taking the first-order terms yields

$$bc_0 m_1 \omega^2 + (1-b)(gm_1)^2 = 0 \tag{20}$$
$$2Ac_0\rho(x_e\omega^2 - g) - (1-b)(gm_1)^2 = 0 \tag{21}$$

with solutions

$$\omega_1^2 = \frac{g^2\left(m_1^2 + 2Am_1\rho x_e + 2Ac_0\rho/g - \sqrt{8A\rho x_e m_1^3 + \left(m_1^2 - 2A\rho x_e m_1 + 2Ac_0\rho/g\right)^2}\right)}{4Ac_0\rho x_e} \tag{22}$$

$$b_1 = \frac{\left(m_1^2 - 2A\rho x_e m_1 + 2Ac_0\rho/g + \sqrt{8A\rho x_e m_1^3 + \left(m_1^2 - 2A\rho x_e m_1 + 2Ac_0\rho/g\right)^2}\right)}{2m_1^2} \tag{23}$$

and

$$\omega_2^2 = \frac{g^2\left(m_1^2 + 2Am_1\rho x_e + 2Ac_0\rho/g + \sqrt{8A\rho x_e m_1^3 + \left(m_1^2 - 2A\rho x_e m_1 + 2Ac_0\rho/g\right)^2}\right)}{4Ac_0\rho x_e} \tag{24}$$

$$b_2 = \frac{\left(m_1^2 - 2A\rho x_e m_1 + 2Ac_0\rho/g - \sqrt{8A\rho x_e m_1^3 + \left(m_1^2 - 2A\rho x_e m_1 + 2Ac_0\rho/g\right)^2}\right)}{2m_1^2}. \tag{25}$$

The argument to the square root is always positive, so b_1 and b_2 are always real. Clearly $b_1 > 0 > b_2$, so solution (b_1, ω_1) has the the piston and liquid in phase, and (b_2, ω_2) has them in opposite phase. The argument to the square root can also be written

$$\left(m_1^2 + 2Am_1\rho x_e + 2Ac_0\rho/g\right)^2 - (16A^2 c_0 m_1 \rho^2 x_e)/g$$

from which it follows that ω_1 and ω_2 are always real, with $0 < \omega_1 < \omega_2$. The low frequency oscillation has the liquid and piston in phase, and the high frequency one in opposite phase.

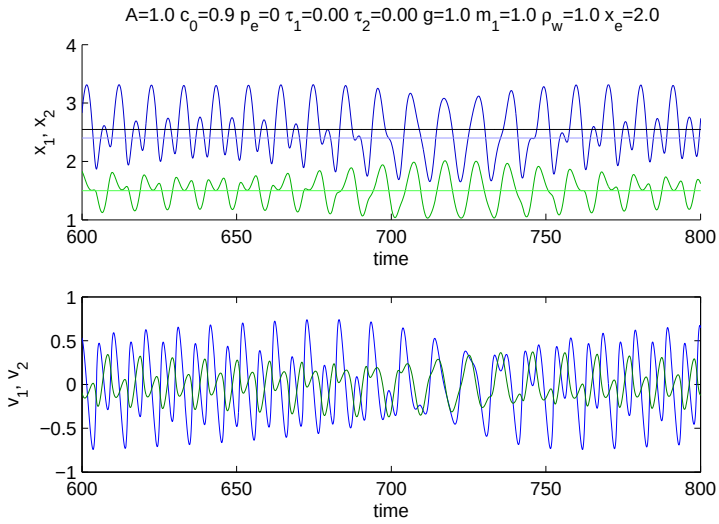

Figure 2: Time series of simulated Dines manometer. The upper panel shows the float (blue) and liquid (green) position, and the lower panel shows the respective velocities. The lighter lines in the upper panel show the equilibrium positions of the float and liquid x_{1e} and x_{2e}, and the black line shows the mean position of the float (calculated over a much longer period than that shown here). Parameters are $A = 1, c_0 = 0.9, g = 1, m_1 = 1, \rho = 1, \tau_1 = \tau_2 = \tau_3 = 0, x_e = 2$. The initial condition was $x_1 = x_{1e} + c_0/(gm_1)$, $x_2 = x_{2e}$ and $v_1 = v_2 = 0$.

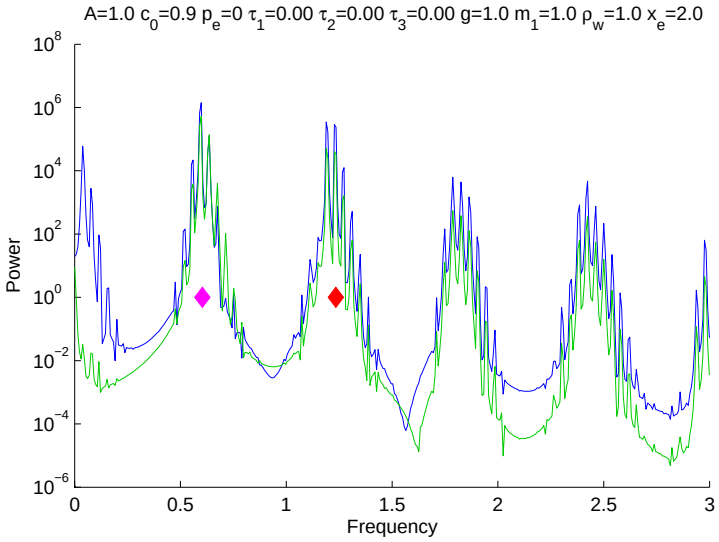

Figure 3: Power spectra of x_1 (blue curve) and x_2 (green curve) from the simulation in Fig. 2. The diamonds indicate the frequencies for the coupled oscillation, ω_1 (magenta) and ω_2 (red).

A time-series plot of simulated motion for the full equations is shown in Fig. 2. This example clearly shows periods where the liquid and piston oscillate in phase (e.g. 690 – 770), and periods where they are out-of-phase. Apparently both oscillations are present and beating is occurring, but see further discussion of this case later. The mean position of the float (black line) is significantly displaced from its equilibrium position x_{1e} (lighter blue line). In the usual anemometer parlance, the instrument is overspeeding; that is, the measured mean wind speed has a positive bias. In contrast, the mean liquid position is indistinguishable from x_{2e} (light green line).

The power spectra of x_1 and x_2 for this simulation are shown in Fig. 3, with the coupled frequencies ω_1, ω_2 indicated by the filled diamonds. The spectrum is dominated by a broad peaks around $\omega_1 \approx 0.6037$, $\omega_2 \approx 1.2347$, and the harmonics thereof. The nonlinearity is evident from the relatively large amplitudes of the harmonics, and from the broadness of the peaks. The broad peaks are also notably spiky; in this example the spikes are spaced at about 0.04, but when run at lower amplitude they become fewer and are spaced at $0.027 \approx \omega_2 - 2\omega_1$, suggesting that the spikes are the result of nonlinear interactions between the frequencies ω_1 and ω_2. Reducing the amplitude of the oscillations by changing the initial condition leads to narrower spectral peaks and fewer spikes, confirming the role of nonlinearity. There is significant power in the motion of the piston, but not the liquid, at frequencies

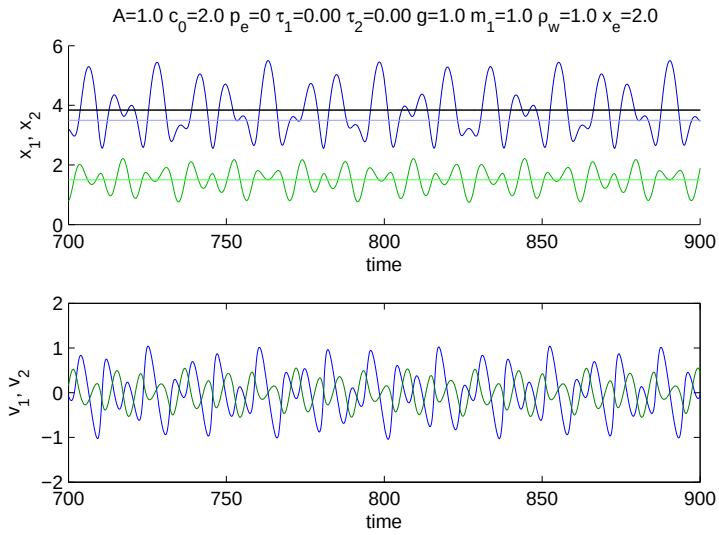

Figure 4: As for Fig. 2, but with $c_0 = 2$.

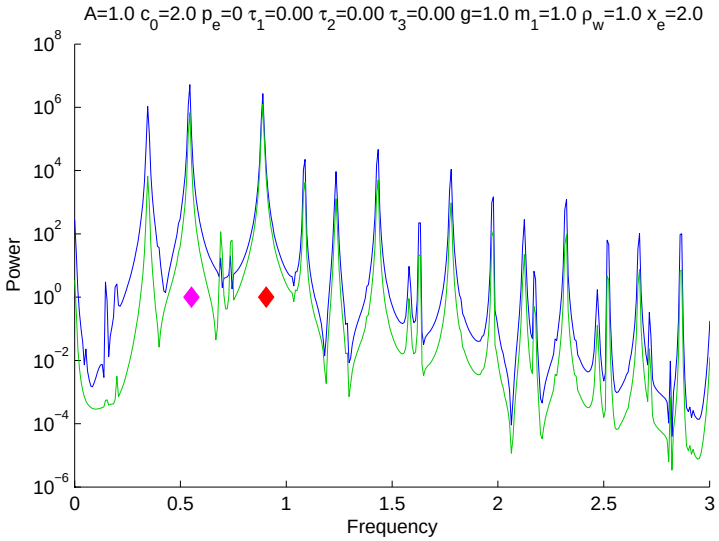

Figure 5: As for Fig. 3, but with $c_0 = 2$.

below 0.3, while the power is more similar for other peaks in the spectrum. The high piston energy and partial decoupling of float and liquid at low frequencies are less apparent when the overall amplitudes are reduced, again implying that nonlinearity may be the cause. This behaviour will be further discussed below.

Limiting behaviour at very high wind speeds, (i.e. the limit $c_0 \to \infty$), is that $\omega_1^2 \to 0$, $b_1/c_0 \to 2A\rho/(gm_1^2)$, $\omega_2^2 \to g/x_e$ and $b_2/c_0 \to 0$. The in-phase oscillation becomes slow and predominantly in the piston, while the opposite-phase essentially becomes independent of the piston and similar to the f_2 case above.

If c_0 is increased from that shown in Fig. 2, then the character of the motion changes. Time-series and spectra for $c_0 = 2$ are shown in Figs 4 and 5. The motion is approximately periodic with the section shown apparently beginning to repeat at about $t = 830$. The spectrum has many more peaks, but the linear analysis describes the strongest two. The offset of the mean float position from x_{1e} persists.

Further indication of the complexity is provided by Fig. 6, which shows the power spectra for a range of c_0. It is clear that the linear analysis successfully picks out the dominant peaks ω_1 and ω_2 (white dotted curves), with their difference being the third prominent peak (black dotted curve). A rich range of harmonics and interharmonics are also apparent. The high power at low frequencies seen in Fig. 3

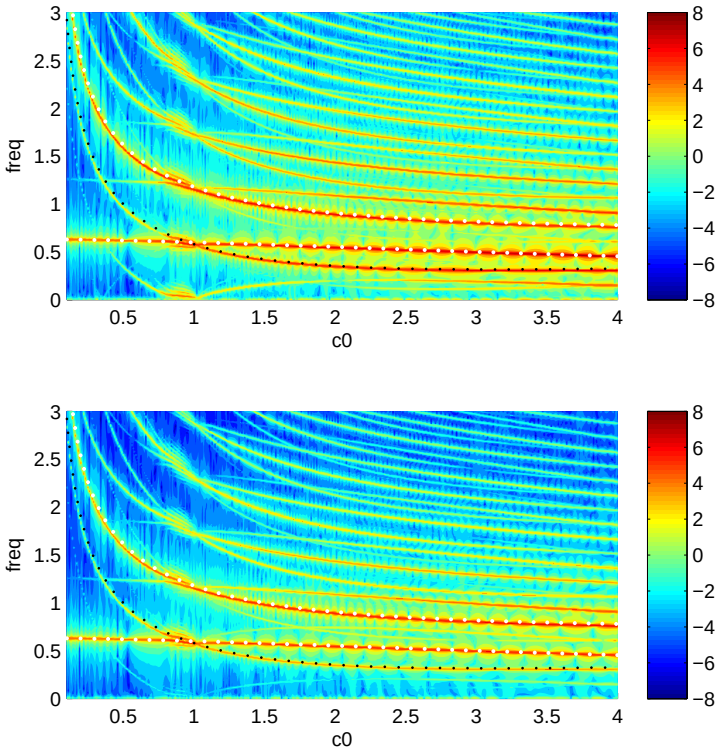

Figure 6: Logarithm base 10 of the power spectral density for x_1 (top) and x_2 (bottom) for values of c from 0.02 to 4 by 0.02. Other parameters are $A = 1$, $g = 1$, $m_1 = 1$, $\rho = 1$ and $x_e = 2$. The dotted white curves are ω_1 (lower) and ω_2 (upper), and the dotted black curve is $\omega_2 - \omega_1$.

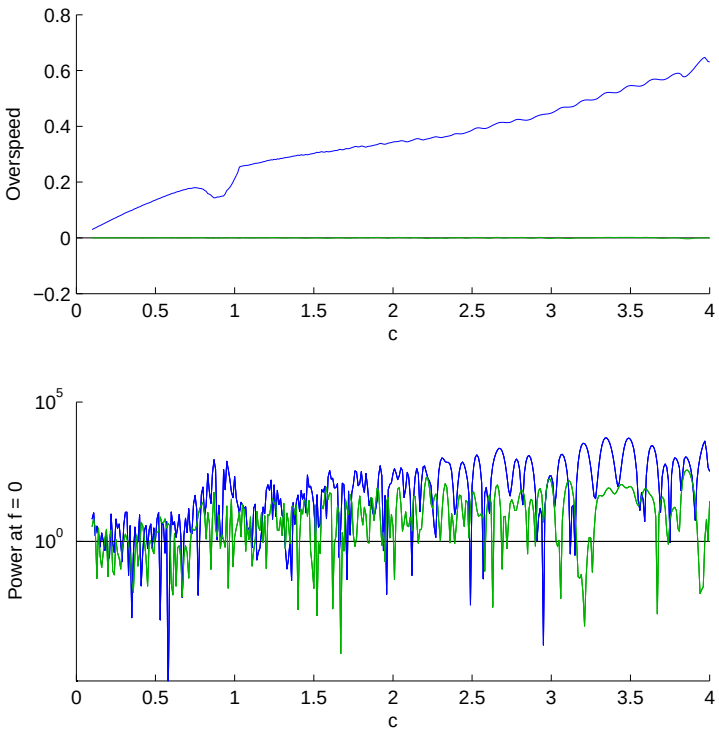

Figure 7: Upper panel: The extent to which the time-mean of x_1 (blue) and x_2 exceed their equilibrium values, in the same simulations as for Fig. 6. That is, $\overline{x_1} - x_{1e}$ (blue) and $\overline{x_2} - x_{2e}$ (green). Lower panel: The power at DC (i.e. $f = 0$) in these simulations.

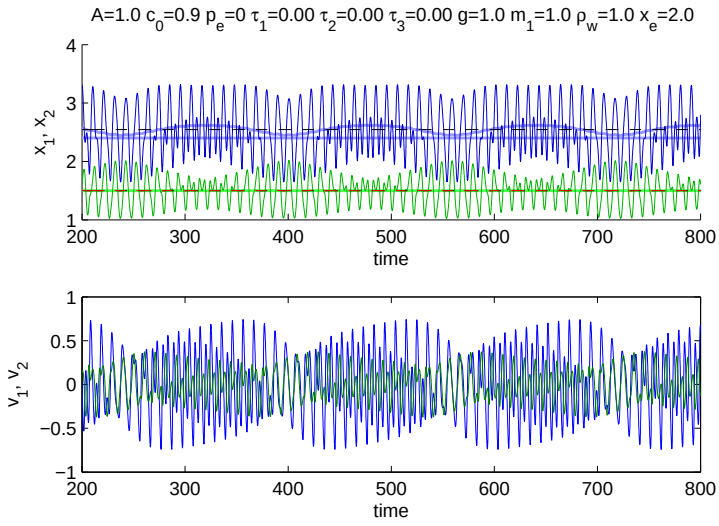

Figure 8: As in Fig. 2, except for a longer period. The thick lighter blue curve shows the low-pass filtered piston positions. The similar green curve is indistinguishable from the water mean position.

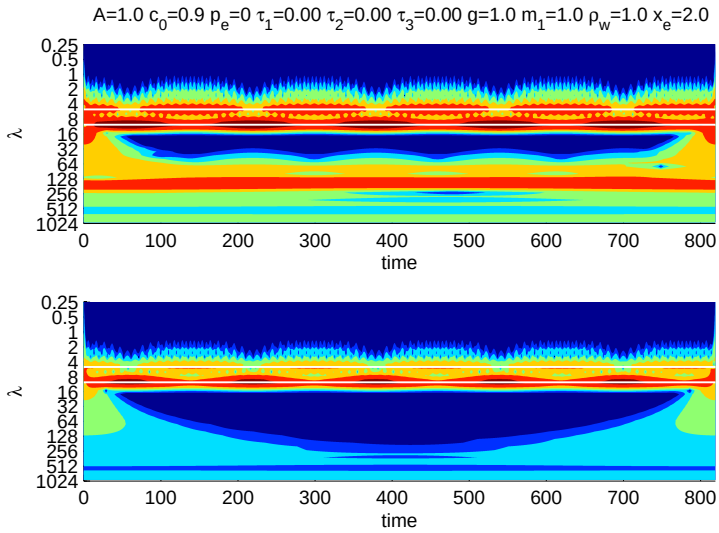

Figure 9: Wavelet power spectrum of the simulation shown in Fig. 2. The upper panel shows the piston motion, and the lower that of the water. The horizontal white lines indicate $\lambda = 2\pi/\omega_1$ and $\lambda = 2\pi/\omega_2$. Note also the much lower frequency oscillation present near $\lambda = 150$.

is apparent in the upper panel near $c_0 = 0.9, f = 0$, from which it seems that its origin is a prominent interharmonic that happened to intersect $f = 0$ at that c_0. This intersection occurred because $\omega_2 \approx 2\omega_1$ around that c_0 (as already noted), a relationship that will presumably tend to favour relatively strong coupling between the two oscillations. The closely-spaced spikes in the spectrum seen in Fig. 3 are also apparent. Other interesting features include the regular variation in the width of the peak about ω_1 and to a lesser extent ω_2 and the remaining lines. Similar variation is also apparent at zero frequency, and is shown more clearly in the lower panel of Fig. 7. The upper panel of that figure shows the overspeeding previously noted in Figs. 2 and 4. Relationships between the two panels are obvious, as is the systematic nature of the overspeeding. Reducing the amplitude of the initial departure from equilibrium by a factor of 10 reduces the overspeeding by about a factor of 60, suggesting that determining the cause of the overspeed will require an analysis of the nonlinearity in the system.

We return now to the case with $c_0 = 0.9$ and consider the cause of the overspeeding. Figure 8 shows a longer version of Fig. 2, which includes also a low-pass filtered float position. This curve is a maximum when the water and piston are most obviously out-of-phase, and a minimum when they are in-phase. The trapped air acts as a nonlinear spring – the force required for a given incremental displacement is larger when the air is already compressed from its equilibrium position, than when it is rarefied. Thus, as the

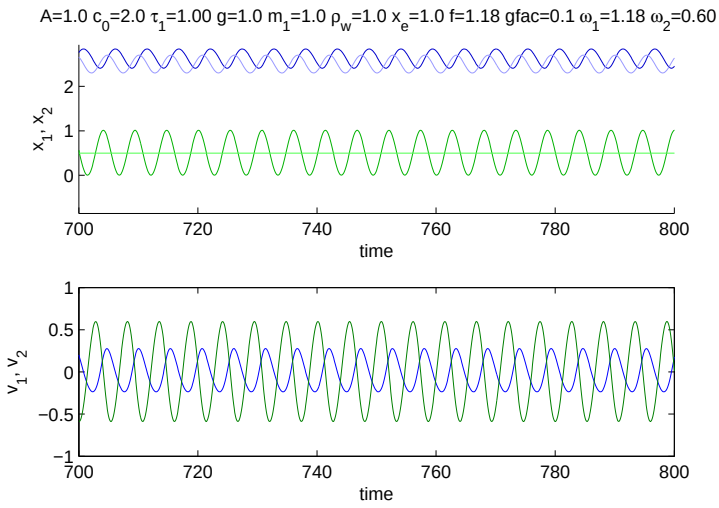

Figure 10: Time series of manometer response for sinusoidally-varying oscillation at frequency $f = \omega_2$. Upper panel, piston (blue) and water (green) positions. Dark curves show the instantaneous positions, and the lighter curves the calibrated values x_{1e} and x_{2e} calculated from $c(t)$. Lower panel, piston and water velocity. Parameters are $A = 1, c_0 = 2, \tau_1 = 1, \tau_2 = \tau_3 = 0, g = 1, m_1 = 1, \rho = 1, x_e = 1$, giving $\omega_1 = 1.18$, $\omega_2 = 0.60$, $b_1 = -0.56$ and $b_2 = 3.56$. The forcing amplitude is $G = 0.1$.

amplitude of the out-of-phase oscillation increases, the piston will experience a nonlinear increase in the upwards force it experiences at the bottom of its cycle, when the water rises to meet it. It appears that this is sufficient to increase its mean position over that that would occur with a smaller-amplitude, more linear, oscillation.

Figure 9 shows the wavelet power spectrum for the piston and water from this simulation. The amplitudes of the two coupled modes are not constant, but cycle slowly with time. Evidently energy is being transferred back and forwards between them. This transfer is accompanied by a much slower oscillation in the piston, but not in the water. The amplitude of this latter oscillation depends on the overall amplitudes in the system, so it is clearly nonlinear in nature. I can recall seeing in the past Dines anemometer traces with an oscillation with a period of several minutes, attributed to gravity waves. Is it possible that this phenomenon is instead a manifestation of this nonlinear effect within the instrument?

2.2 *The effects of damping the float*

A real Dines float has damping due to the viscosity of the water, the shaft from the float protruding through the bushing at the top of the float chamber, from the pen mechanism, and from remote read-outs. Thus such motions will be likely to be damped. On the other hand, the forcing $c(t)$ will vary due to turbulence, not be constant as in section 2.1. The behaviour when the damping $\tau_1 \neq 0$ and c varies in time is now explored. To begin with, c will oscillate sinusoidally,

$$c(t) = c_0[1 + G\sin(ft)] \tag{26}$$

where c_0 is related to the mean wind speed, G is essentially a gust factor, and f is the forcing frequency. The main diagnostic will be to compare the actual oscillation of the piston and water with that expected from the calibration equations, namely the equilibrium values expected for steady forcing. In these simulations, quite heavy damping $\tau_1 = 1$ is applied.

Interesting cases are likely to include those where f is close to one of the dominant frequencies apparent in Fig. 6, perhaps most strongly the opposite-phase oscillation $f = \omega_2$ but note that both coupled linear modes will be directly forced by oscillations in c. A sample time-series for this case is shown in Fig. 10. The water and piston are oscillating roughly in opposite phase, with relative amplitude 0.47, not too far from $|b_2| = 0.56$ for these settings. The amplitude of the piston oscillation is about 7% greater than that expected from the calibration, even with this relatively heavy damping. Evidently resonance is present at this frequency, as expected. More interestingly, the mean piston position is clearly offset slightly above its calibrated value, as also found in some undamped cases. As before,

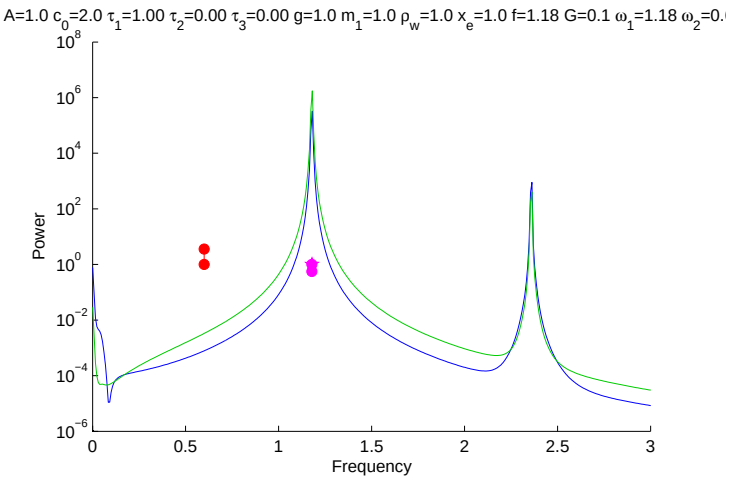

Figure 11: Power spectrum for the simulation in Fig. 10. Symbols as in Fig. 3, with the addition of a magenta pentagram (largely obscured) showing the forcing frequency. The lengths of the dumb-bells at ω_1 and ω_2 indicate the ratios b_1 and b_2.

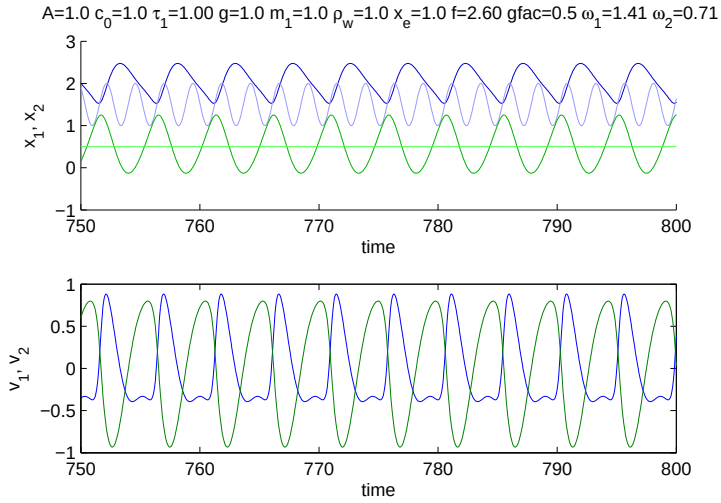

Figure 12: As for Fig. 10, except with $c_0 = 1$, giving $\omega_1 = 1.41$, $\omega_2 = 0.71$, $b_1 = -1$ and $b_2 = 2$. The forcing frequency is $f = 2.6$, roughly twice ω_2 and the amplitude is increased to $G = 0.5$.

the instrument is overspeeding. Examination of the spectrum (Fig. 11) shows the now familiar peak at low frequency. An appealing explanation for the overspeeding is that nonlinearities are generating this peak (and many others), but that the Newtonian damping is unable to remove very low frequency (and in particular, DC) motions. However, this explanation cannot be complete because overspeeding occurs also in the undamped simulations.

More exotic behaviour is possible, in particular in the interesting case where c_0 satisfies $\omega_2 \approx 2\omega_1$. Figure 12 shows such a case forced at a little less than twice ω_2. The amplitude was increased to $G = 0.5$ to really let the nonlinearities rip. The system resonates at $f/2$, *half* the forcing frequency, and overspeeds by about 35%.

The behaviour is summarised in Fig. 13. The energy (panel a) clearly depicts the resonant peak, with the overspeeding of the mean shown in panel (b). Note from panel (c) that the gusts are measured accurately at low frequencies, then tail off rapidly before being overestimated at resonance, then tailing off again. From panel (d), the piston and water oscillations differ in phase by $\sim \pi/3$ at low frequency, and about π at high, with the dividing frequency being that at which the piston ignores the forcing. Increasing the amplitude of the forcing (Fig. 14) increases the amplitude of the response and introduces the second resonant peak already seen in Fig. 12, but does not produce much else in the way of change.

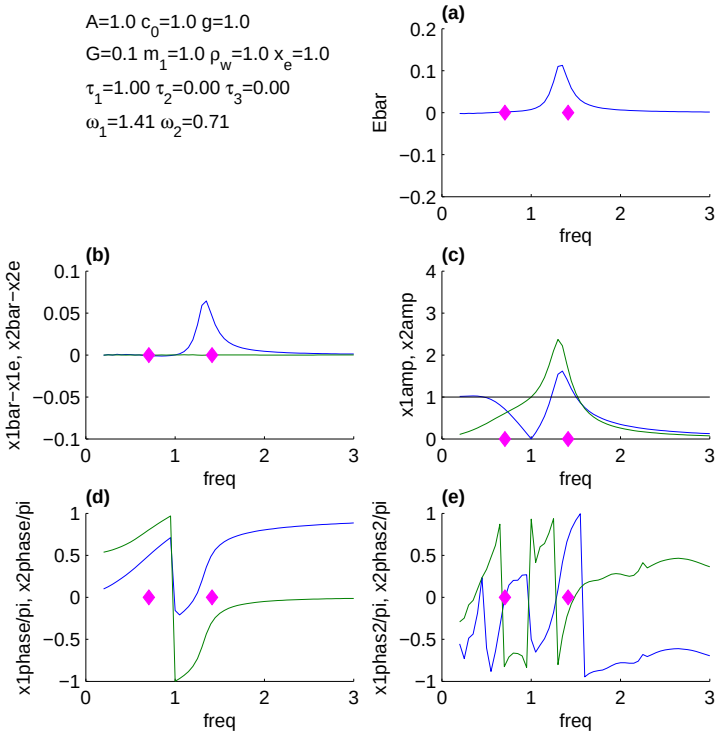

Figure 13: A summary of the behaviour for the forced damped system. Each panel shows the system behaviour as a function of forcing frequency f, with the natural frequencies ω_1 and ω_2 indicated by magenta diamonds. Paremeters are shown at top left. (a): the time-mean total energy in the system, $\overline{E_K} + \overline{E_{P,1}} + \overline{E_{P,2}} + \overline{E_{P,p}}$. (b): the mean piston and water position, relative to that expected for steady forcing c_0. (c): the amplitude of the piston and water oscillations, normalised by the expected piston amplitude from the calibration equations. (d): the phase difference between the forcing and the response. (e): the phase of the first harmonic of the response.

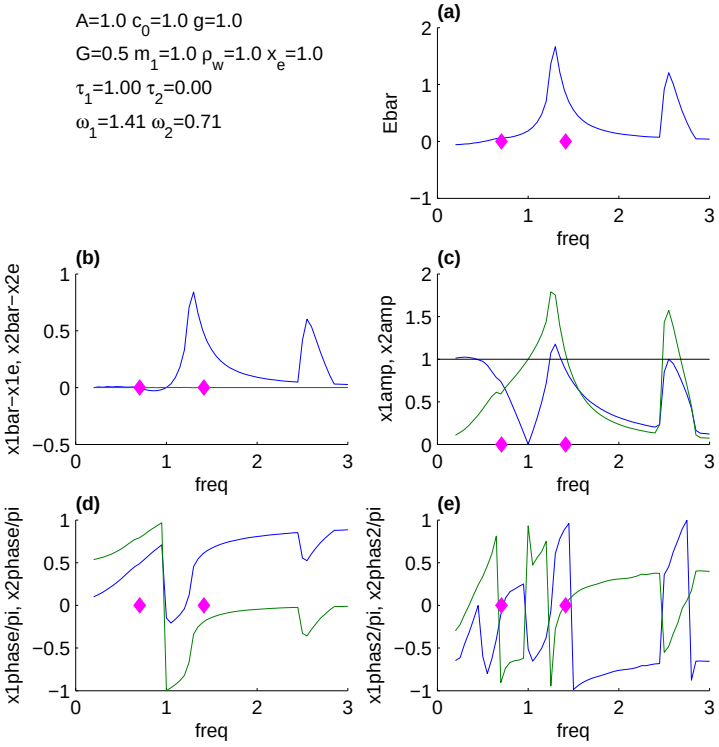

Figure 14: As for Fig. 13, except with $G = 0.5$.

2.3 *Accounting for pressure in the outer chamber*

Including a constant nonzero pressure p_{env} in the outer chamber increases the complexity of the algebra but does not require any change in the method of solution. The equilibrium water position is unchanged, while the float position becomes

$$x_{1e} = x_{2e} + \frac{c_0}{gm_1 + Ap_{env}}. \tag{27}$$

For comparison with the earlier simulations, we define

$$\Delta_0 = c_0 \left(1 + \frac{Ap_{env}}{gm_1}\right)^{-1} \tag{28}$$

which is the length that the trapped air would assume if $p_{env} = 0$. That is, we work in terms of the length or volume of trapped air, rather than its mass. Searching for coupled oscillations following the procedure in section 2.1 reveals that

$$bc_0\omega^2 m_1 + (1-b)(gm_1 + Ap_{env})^2 = 0 \tag{29}$$

and

$$2Ac_0\rho(x_e\omega^2 - g) - (1-b)(gm_1 + Ap_{env})^2 = 0 \tag{30}$$

with solutions

$$\omega_1^2 = \frac{S + 4A\rho x_e(gm_1 + Ap_{env})^2 - \sqrt{S^2 + 8Am_1\rho x_e(gm_1 + Ap_{env})^4}}{4Ac_0 m_1 \rho x_e} \tag{31}$$

$$b_1 = \frac{S + \sqrt{S^2 + 8Am_1\rho x_e(gm_1 + Ap_{env})^4}}{2m_1(gm_1 + Ap_{env})^2} \tag{32}$$

and

$$\omega_2^2 = \frac{S + 4A\rho x_e(gm_1 + Ap_{env})^2 + \sqrt{S^2 + 8Am_1\rho x_e(gm_1 + Ap_{env})^4}}{4Ac_0 m_1 \rho x_e} \tag{33}$$

$$b_2 = \frac{S - \sqrt{S^2 + 8Am_1\rho x_e(gm_1 + Ap_{env})^4}}{2m_1(gm_1 + Ap_{env})^2} \tag{34}$$

where

$$S = (gm_1 + Ap_{env})^2(m_1 - 2A\rho x_e) + 2Agm_1\rho c_0 \tag{35}$$

It follows from

$$\begin{aligned}[S + 4A\rho x_e(gm_1 + Ap_{env})^2]^2 - [S^2 + 8Am_1\rho x_e(gm_1 + Ap_{env})^4] \\ = 16A^2 c_0 g m_1 (gm_1 + Ap_{env})^2 \rho^2 x_e \\ > 0\end{aligned} \tag{36}$$

that $\omega_1^2 > 0$, so ω_1 is real.

Physically, the effect of including p_{env} is to increase the stiffness of the spring. Previously, if the volume of the trapped air halved, then p doubled. Now, p becomes $2(p_{env} + p) - p_{env} = p_{env} + 2p$. For $p_{env} \gg p$, as will usually be the case, this makes a big difference to the restoring force. The main effect will be to shift the oscillations to higher frequency.

Figure 15: Photograph of the lower end of a Dines anemometer float, showing the choke. The pressure tube enters up the hole in the middle, almost filling it.

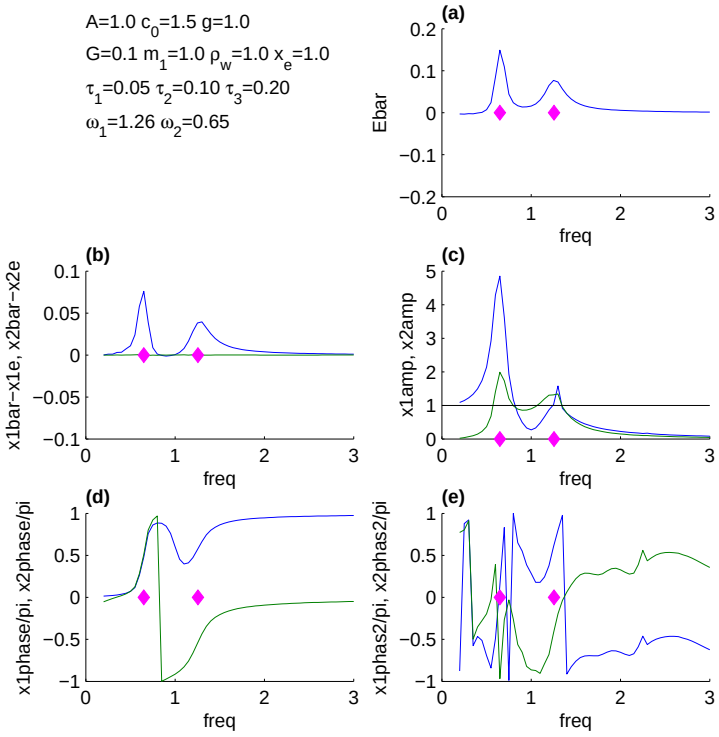

Figure 16: As for Fig. 13, except with settings as shown in the upper left. In particular, the absolute motions of the piston and water are weakly damped, while the relative motion is more strongly damped.

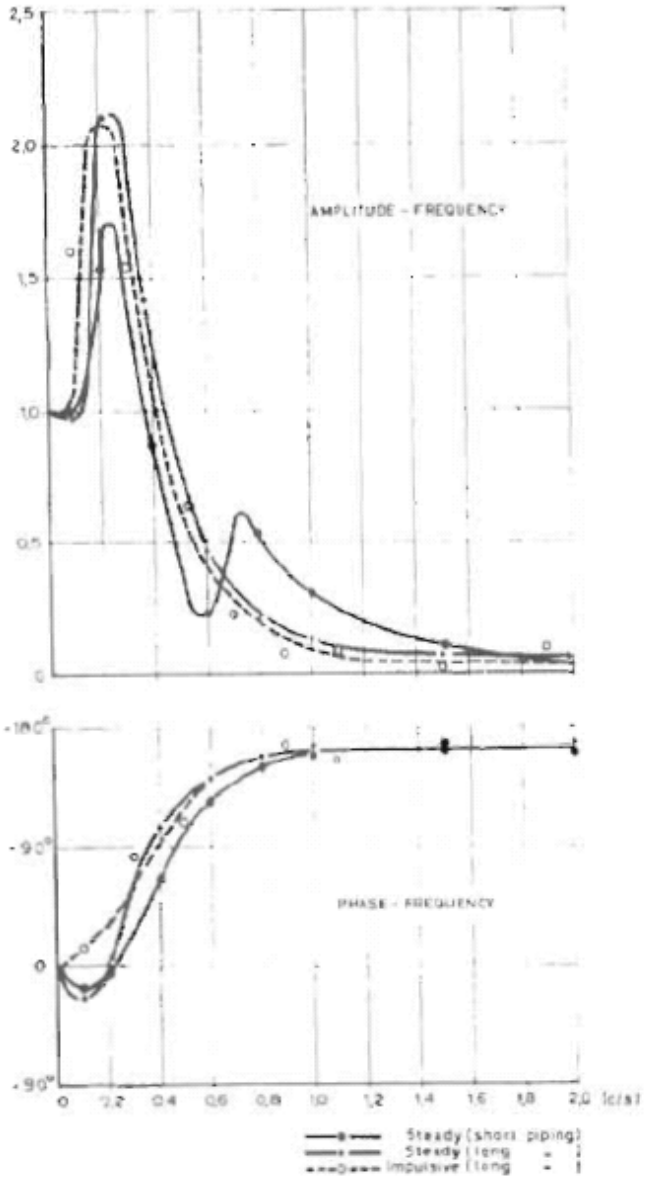

Figure 17: The relative amplitude (top) and phase (bottom) of the float movement, as a function of forcing frequency, for a variety of tubing lengths. Reproduced from Borges (1968, Fig. 5).

2.4 *Damping the relative motion*

In a real Dines anemometer, the bottom of the float is not open, but contains a constriction, shown in Fig. 15. For convenience, we call this constriction the Dines choke. We have not been able to discover any literature on this feature, and so the reasons for its inclusion in the design are unclear. However, it will clearly have a damping effect on the relative motions of the float and the liquid, and was the motivation for the inclusion of the damping with time-scale τ_3 in Eqs. (3) and (5).

Figure 16 presents plots summarising the response of the model to sinusoidal forcing of various frequencies, with $\tau_3 \neq 0$. It is clear that the out-of-phase resonance is weaker than the in-phase, with these settings, as is physically reasonable. Borges (1968) conducted laboratory experiments with a pressure-tube anemometer float chamber, in which sinusoidal pressure forcing was applied. He presented a graph showing the amplitude and phase of the float response, reproduced here as Fig. 17. Clearly, this figure is in good agreement with panels b and d of Fig. 16. Note that Borges (1968) presented results for several different mean wind speeds. Variation in the mean wind speed changes the mean mass of trapped air c_0, and hence the resonant frequencies ω_1 and ω_2. The results of Borges suggest that the magnitude of the out-of-phase resonance is wind-speed dependent, consistent with this sensitivity to c_0, but full investigation of this phenomenon in the model awaits further investigation.

3. Discussion

A simplified model of the Dines anemometer has been developed. Solution of the linearised equations reveal two fundamental frequencies, corresponding to oscillations in which the water and float are either exactly in or exactly out of phase. The former oscillation has the lower frequency. Numerical solutions reveal that the linear solution well captures the dominant frequencies, and that the numerical solutions contain additionally a rich array of harmonics and interharmonics of the linear frequencies. Nonlinearity in the out-of-phase oscillation leads to a positive bias in the mean measurement (overspeeding), the magnitude of which depends on the amplitude of the oscillation. Under certain circumstances, a third oscillation, of much lower frequency, can occur and is related to a regular transfer of energy between the in-phase and out-of-phase oscillations.

Numerical solutions of the forced damped equations reveal that resonances can occur at one or both of the linear frequencies, depending on the precise circumstances. The amplitude of these resonances can be greater than that suggested through the calibration equations by the amplitude of the forcing. That is, the magnitude of gusts at these resonant frequencies may be overestimated. The model is capable, with some tuning of the unknown parameters, of at least qualitatively reproducing the results of previous laboratory investigations that reported these resonances.

In this context, it is interesting to note the analysis of gust frequency at Australian observing sites by Cechet and Sanabria (2010). They studied sites with long records both pre- and post- the period during which the Australian Bureau of Meteorology was replacing Dines anemographs with cup anemometers at such sites. Cechet and Sanabria (2010) show that strong gusts were much more prevalent in the Dines anemometer era than in the cup anemometer era. The resonances in the Dines float chamber, identified here, seems to be a likely explanation for the greater measured gustiness in the Dines era.

This is a preliminary report of work in progress. Colleagues at the Cyclone Testing Station at James Cook University are currently undertaking laboratory and field measurements on some remaining Dines anemometers owned by the Bureau of Meteorology. These measurements will be used to calibrate an improved version of the model described herein. The main improvement planned is to remove the simplifications to the float geometry. The final, calibrated, anemometer model will be coupled to a model that produces synthetic turbulent wind time series, to allow further investigation of the record gusts in Tropical Cyclones Tracy, Vance, and possibly others.

Several earlier studies (e.g. Sanuki 1952) have noted resonance in the system, without analysing the

float dynamics as here. Some of these studies note that the resonant frequency depends on the length and diameter of the tubing from the pitot-tube head (e.g. Goldie 1935; Borges 1968). The explanation for this phenomenon has been though to be some form of resonance in the tubing, but another possibility is that variations in the tubing correspond to variations in the mass of the trapped air, which would change the resonant frequencies by changing the effective spring constant. It is hoped that the laboratory measurements, in conjunction with the improved model, will answer this question.

Finally, it is hoped that the model will reach a degree of verisimilitude such that it can be used to determine whether or not the record gust measurements in Severe Tropical Cyclones Tracy and Vance were affected by resonances in the float system. Answering this question is critical to making informed use of these measurements for purposes including risk assessment and engineering design.

Acknowledgements

This work is partly supported by the Australian Department of Climate Change. I am grateful to Jeff Callaghan, John Ginger, Bruce Harper, David Henderson, John Holmes and Ian Muirhead for helpful and interesting discussions about the Dines anemometer. I particularly thank Craig Miller for a making available a very useful unpublished bibliographic review of the Dines anemometer and for providing copies of some obscure references, which greatly helped to focus the research presented herein. I especially thank David Edwards for an informative and frank hands-on demonstration of a Dines anemometer, and him and Paul Leigh for their help with borrowing an instrument for further investigation.

References

Borges, A. R. J., 1968: On the frequency response of floater-type anemographs (velocity fluctuations in the direction of mean speed). *Technica*, **379**, 505–511.

Bureau of Meteorology, 1987: Effects on the Performance of a 150 knot Dines anemograph. Instrument Test Report No. 600, Commonwealth of Australia.

Cechet, R. P. and L. A. Sanabria, 2010: Extreme-value time-series analysis of Australian Region A gust wind speeds to examine instrument bias. *Proceedings of the AMOS Annual Conference, Canberra, Australia*, Australian Meteorological and Oceanographic Society.

Dines, W. H., 1892: Anemometer comparisons. *Quart. J. Roy. Meteor. Soc.*, **18**, 165–185.

Dyck, H. D., 1941: Comparison of extreme gust velocities as recorded by the Dines anemometer and 5-minute velocities as recorded by the Robinson anemometer. *Mon. Wea. Rev.*, **69**, 301–302.

Gold, L.-C. E., 1936: Wind in Britain – The Dines anemometer and some notable records during the last 40 years. *Quart. J. Roy. Meteor. Soc.*, **62**, 167–206.

Goldie, A. H. R., 1935: Wind records from the Bell Rock Lighthouse. *Geophysical Memoirs*, **63**.

Handcock, D. E., 1963: Comparison of speeds of response of Dines anemograph and electrical recording cup generator anemometer. Instrument test report no 511, Commonwealth Bureau of Meteorology.

Logue, J. J., 1986: Comparison of wind speeds recorded simultaneously by a pressure-tube anemograph and a cup-generator anemograph. *Met. Mag.*, **115**, 178–185.

Mattice, W. A., 1938: A comparison between wind velocities as recorded by the Dines and Robinson anemometers. *Mon. Wea. Rev.*, **66**, 238–240.

Sanuki, M., 1952: A new development of the theoretical and experimental lag of Dines pressure tube exposed in fluctuating winds. *Papers in Meteorology and Geophysics*, **3**, 115–124.

Smith, S. G., 1981: Comparison of wind speeds recorded by pressure-tube and Meteorological Office electrical cup generator anemographs. *Met. Mag.*, **110**, 288–300.

Wieringa, J., 1980: The mystery of the hicupping Dines anemometer. Report v-356, KNMI, De Bilt.